MATHEMATICS

Mechanical manipulation for ordered topological defects

Ziyan Gao[1]†, Yixuan Zhang[1], Xiaomei Li[2], Xiangping Zhang[1], Xue Chen[3], Guoshuai Du[4], Fei Hou[4], Baijun Gu[1], Yingzhuo Lun[1], Yao Zhao[1], Yingtao Zhao[1], Zhaoliang Qu[5], Ke Jin[4], Xiaolei Wang[6], Yabin Chen[4], Zhanwei Liu[1], Houbing Huang[4], Peng Gao[2], Maxim Mostovoy[7], Jiawang Hong[1]*, Sang-Wook Cheong[8], Xueyun Wang[1]*

Randomly distributed topological defects created during the spontaneous symmetry breaking are the fingerprints to trace the evolution of symmetry, range of interaction, and order parameters in condensed matter systems. However, the effective mean to manipulate topological defects into ordered form is elusive due to the topological protection. Here, we establish a strategy to effectively align the topological domain networks in hexagonal manganites through a mechanical approach. It is found that the nanoindentation strain gives rise to a threefold Magnus-type force distribution, leading to a sixfold symmetric domain pattern by driving the vortex and antivortex in opposite directions. On the basis of this rationale, sizeable mono-chirality topological stripe is readily achieved by expanding the nanoindentation to scratch, directly transferring the randomly distributed topological defects into an ordered form. This discovery provides a mechanical strategy to manipulate topological protected domains not only on ferroelectrics but also on ferromagnets/antiferromagnets and ferroelastics.

INTRODUCTION

Topological defects exist in a variety of solid-state systems, serving as profound relics to understanding continuous phase transition (*1*–*8*). Not like the ordered textures in well-confined nanodots, nanorods, superlattices, and heterostructures (*9*–*11*), the topological defects are usually randomly distributed in bulk single crystals, as visualized in bulk superconductors (*12*, *13*), ferromagnets (*14*, *15*), and ferroelectrics (*16*, *17*). Focusing on the ferroelectric realm, the topological defects are spatially constructed by the various orientations of electric dipoles, forming exotic domain/domain wall (*18*, *19*), polar screw/vortex (*4*, *20*, *21*), skyrmion (*22*–*24*), meron (*25*), etc., which lead to a tantalizing area so-called "topotronics," combining spatial topology and emerging physical phenomena. Among typical ferroelectrics, hexagonal manganites (h-$RMnO_3$, R = Y, Ho-Lu) exhibit three distinguishable types of domains: stripe, loop, and vortex, which are critically determined by the annealing temperature relative to the Curie temperature (T_C) (*26*). The topological ferroelectric domain wall hosts various physical properties such as stabilized charged domain walls (*27*, *28*), half-wave rectification (*29*, *30*), and high carrier mobility at the domain wall (*31*, *32*), which has potential application in multi-states memory, nano-electronic devices, and sensors. To realize these multifunctional properties, effective manipulation of the spatial arrangement of the domain wall is critical (*2*, *33*–*38*). In particular, rather deterministic control of domain wall orientation and density in hexagonal manganites is not realized so far.

Here, we artificially created nanoindentations/nanoscratches on the surface of samples with nanoindentation apparatus. The residual strain was introduced at room temperature and then subjected to a high-temperature annealing process to achieve precise local directional regulation of vortex domain. On the basis of the designing strategy of strain-induced Magnus force, two antiparallel scratches are introduced to realize high-density parallel mono-chirality stripe domains between the nanoscratches, with a periodicity of 400 nm. Raman and scanning transmission electron microscopy (STEM) measurements were used to characterize the strain distribution near nanoscratches, and the underlying mechanism was analyzed.

RESULTS

High-temperature annealing across T_C ($T > T_C = 1400$°C for $LuMnO_3$) of hexagonal manganites crystal induces randomly distributed ferroelectric vortex domains, as shown in Fig. 1A. Because of the lattice distortion and trimerization, the vortex domains form $Z_2 \times Z_3$–type vortex-antivortex pairs, as characterized by ($\alpha+$, $\beta-$, $\gamma+$, $\alpha-$ $\beta+\gamma-$) and ($\alpha+$, $\gamma-$, $\beta+$, $\alpha-$, $\gamma+$, $\beta-$) with reversed vorticity. The vortex cores are robust, while the domain walls are controllable in the presence of external electric field (*33*, *34*). It has been demonstrated that the vortex domains can be unfolded into mono-chiral topological stripes through high-temperature straining, via the opposite motion of vortices and antivortices (*38*), which suggests that the strain/strain gradient is an effective means to manipulate the vortex cores. The latest research endeavors extend this concept to pressure-driven domain engineering, substantiating that applied pressure at high temperature can indeed regulate the frequency and orientation of the induced stripe-like domains (*39*). However, high-temperature straining is rather inaccessible and highly uncontrollable. Here, different from the applied stress near the phase transition temperature

[1]School of Aerospace Engineering, Beijing Institute of Technology, Beijing 100081, China. [2]Electron Microscopy Laboratory and International Center for Quantum Materials, School of Physics, Peking University, Beijing 100871, China. [3]Engineering Research Center for Semiconductor Integrated Technology, Institute of Semiconductors, Chinese Academy of Sciences, Beijing 100083, China. [4]Advanced Research Institute of Multidisciplinary Science, Beijing Institute of Technology, Beijing 100081, China. [5]Institute of Advanced Structure Technology, Beijing Institute of Technology, Beijing 100081, China. [6]Department of Physics and Optoelectronics, Faculty of Science, Beijing University of Technology, Beijing 100124, China. [7]Zernike Institute for Advanced Materials, University of Groningen, Nijenborgh 4, 9747 AG Groningen, Netherlands. [8]Rutgers Center for Emergent Materials and Department of Physics and Astronomy, Rutgers University, 136 Frelinghuysen Road, Piscataway, NJ 08854, USA.
*Corresponding author. Email: xueyun@bit.edu.cn (X.W.); hongjw@bit.edu.cn (J.H.)
†Present address: School of Materials Science and Engineering, Peking University, Beijing 100871, China.

(T_C) (*40*), to demonstrate a room temperature strain/strain gradient designing strategy, the nanoindentation technique is used to create an indent with a typical Berkovich indenter on the surface of as-grown $LuMnO_3$ single crystal to induce local stress/strain distribution, as displayed in Fig. 1B. Followed by a high-temperature annealing across T_C, the induced strain gives rise to a rearrangement of the topological ferroelectric vortex. The sequence of annealing procedure is schematically shown in fig. S1. After annealing, a sixfold symmetric domain distribution around the indent is revealed by chemical etching and optical imaging, as presented in Fig. 1C. This suggests that the room temperature nanoindentation-introduced strain/strain gradient dominates the arrangement of created vortices during the high-temperature annealing.

The possibility that the sixfold symmetric domain distribution is induced by the symmetry of indenter shape (Berkovich indenter with threefold symmetry) is ruled out by comparing identical experiments by a spherical indenter (with rotational symmetry), as shown in Fig. 1D. Phase-field simulations (Fig. 1, E and F, and fig. S2) further confirm the sixfold symmetry of domain distribution by different shapes of indenters. These experiments and simulations suggest that the hexagonal crystalline structure and the strain field around the indent dominate the domain evolution. To reveal the underlying mechanism, the interaction energy $\mathbf{F}_{\text{int}}$ between strain field and the vortex-antivortex positions is considered (*38*)

$$\mathbf{F}_{\text{int}} = \frac{\pi}{3}\lambda h[(\varepsilon_{xx} - \varepsilon_{yy})(y_A - y_V) + 2\varepsilon_{xy}(x_A - x_V)] \quad (1)$$

where (x_V, y_V) and (x_A, y_A) are the Cartesian coordinates of the vortex and antivortex, respectively. ε_{ij} is the strain tensor. λ is the energy coupling coefficient, and h is the thickness of the sample. The Magnus-type force applied to the vortex and antivortex can be obtained by taking differential concerning their Cartesian coordinates

$$f_V = -\frac{\partial \mathbf{F}_{\text{int}}}{\partial x_V} = -f_A = \frac{\pi}{3}\lambda h\left[2\varepsilon_{xy}, (\varepsilon_{xx} - \varepsilon_{yy})\right] \quad (2)$$

This Magnus-type force pulls the vortex and antivortex cores apart from each other. For clarity, we plot the Magnus-type force acquired from the plastic deformation, as given in Fig. 1G and enlarged first quadrant area in Fig. 1H. Visually, we can tell that the alternating Magnus force distribution shows a threefold symmetry, which divides the area around the indent into six areas (see fig. S3 for detailed discussion of Magnus force distribution). The six regions are separated radially by the six principal directions, while the Magnus-type forces within the region are mainly distributed tangentially, as indicated by the black and white dashed arrows in Fig. 1H. Figure 2A shows the movement process of vortex and antivortex cores that forms a sixfold symmetric distribution. Subjected to the tangent Magnus force, vortex and antivortex cores alternately accumulate near the six principal directions (1, 3, and 5 for antivortices; 2, 4, and 6 for vortices). In contrast, the main component of Magnus forces along the principal directions is radial. As a result, the local vortex (antivortex) cores move away from (close to) the indent along the six principal directions. Eventually, under the simultaneous action of the tangential and radial Magnus forces, a sixfold symmetric domain distribution is generated (fig. S4). The phase-field simulation (Fig. 2, B to E, and fig. S5) displays the evolution process, suggesting the opposite movement of vortex and antivortex cores. Additional nanoindentation experiments with different loading forces (figs. S6 and S7) have confirmed the excellent reproducibility and also demonstrated that the periodicity of domain distribution is reduced as the mechanical load increases. It is worth noting that the orientation of the sixfold symmetric distribution is consistent even if the indenter is pushing in different orientations, highlighting that the induced strain distribution is coupled to the hexagonal crystalline lattice. The finite element simulation in Fig. 2F and analytical solution of transversely isotropic crystal pressed by spherical indenters in fig. S8 also confirm that the Magnus force distribution is in threefold symmetry. This mechanism motivates us to propose a precise control of the distribution of the topologically protected vortex domains by nanoindentation.

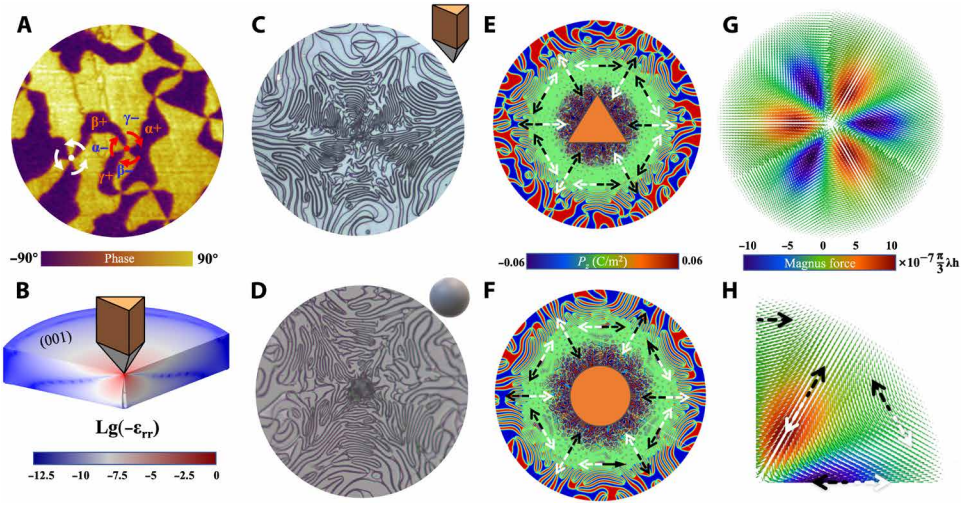

Fig. 1. Nanoindentation induced symmetric distribution of vortex domains on (001) plane. (**A**) Randomly distributed topological ferroelectric domains and vortex-antivortex pairs; the radius of the circular area is 5 μm. (**B**) Finite element method calculated strain distribution introduced by nanoindentation. (**C** and **D**) Optical images of the sixfold symmetrical distribution of vortex domains induced by Berkovich indenter loading at 400 mN and spherical indenter loading at 400 mN, respectively. The radius of the circular area is 140 μm. (**E** and **F**) Phase-field simulated sixfold symmetrical domain distribution by Berkovich and spherical indenters. The radius of the circular area is 150 nm. (**G**) Magnus-type force distribution around the nanoindentation. The arrows indicate the direction of Magnus-type force f_A. (**H**) Enlarged view of the first quadrant of (G). The white and black arrows indicate the main component direction of Magnus forces f_V and f_A, respectively.

On the basis of the above analyzed mechanism of nanoindentation, we extend the vortex domain manipulation to a larger area (fig. S9). To create a relatively larger range of strain/strain gradient distribution, a nanoscratch can be achieved by moving the indenter along a certain direction with a constant mechanical load as seen in Fig. 3B. After the identical annealing process, the nanoscratch gives high-density stripe domains (Fig. 3). Because of the trailing effect of the strain introduced during the scratching process, the domain distributions at the start and end points are different (Fig. 3, A and C). The end point without trailing effect maintains a sixfold symmetry. The orientation of the stripes at the middle area of scratch is at a certain angle to the nanoscratch direction (Fig. 3D), which is attributed to the Magnus-type force distribution induced by nanoindentation according to finite element simulation in fig. S10. In addition, the distribution range of the nanoscratch-induced stripes expands under larger loads, as expected in fig. S11, which suggests the tunability of the strain-influenced range.

In light of the nanoscratch strategy, we design two antiparallel nanoscratches with a distance of 50 μm, as shown in Fig. 3E. The high-density stripes are well aligned between the nanoscratches (Fig. 3, F and G). The periodicity of stripe domains is determined to be 400 nm from the enlarged view and fast Fourier transform in Fig. 3 (H and J). Both ends of the stripe domains are still topological protected ferroelectric vortex with six domains converging (Fig. 3I). The vortex and antivortex cores are pushed to the nanoscratch, which is consistent with the expectation of the design strategy in

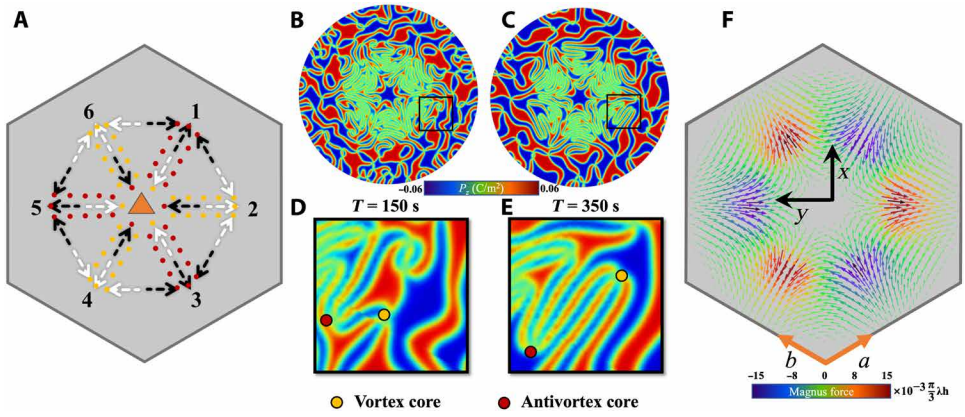

Fig. 2. Formation and evolution of sixfold symmetrical vortex domain distribution. (**A**) Schematic diagram of vortex and antivortex cores movement under Magnus forces. The white and black arrows indicate the main component direction of Magnus forces f_V and f_A, respectively. (**B** and **C**) Sixfold symmetrical domain distribution by phase-field simulation with different evolving times as the indenter pressing (radius of circular area is 100 nm). (**D** and **E**) Enlarged view of black-boxed regions in (A) and (B). (**F**) Magnus force distribution obtained by finite element simulation. The black arrows are Cartesian coordinates on $LuMnO_3$ single crystal, with lattice matrix vector coordinate (*a* and *b*) in orange color.

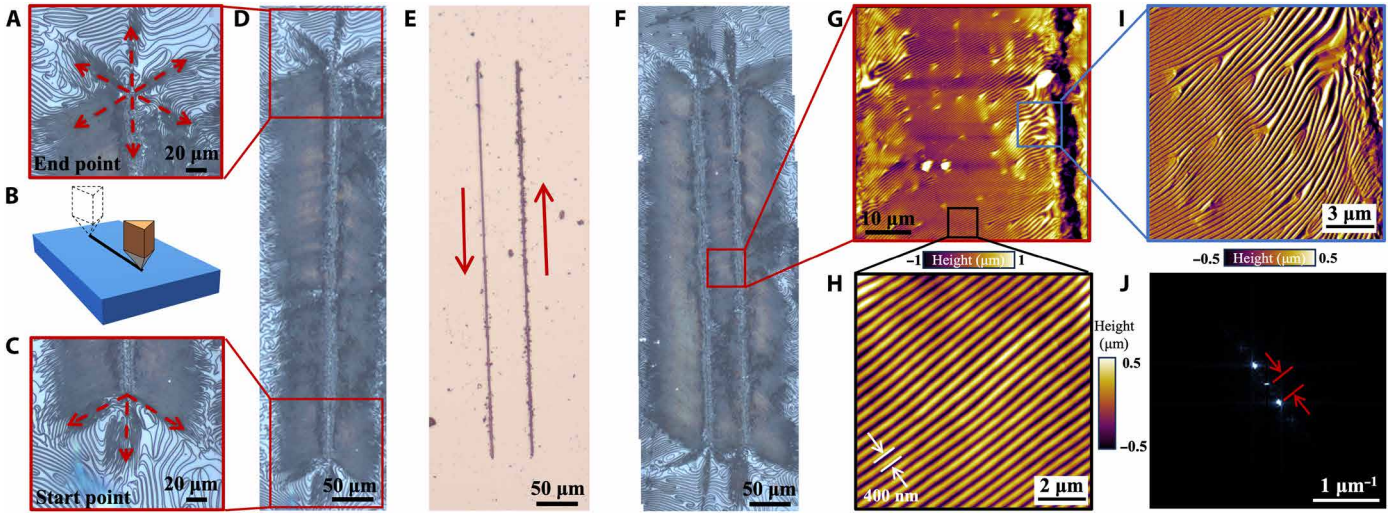

Fig. 3. High-density stripe domains induced by nanoscratches. (**A** and **C**) Enlarged optical images of the start point and end point of the nanoscratch, as schematically shown in (**B**). (**D**) High-density stripe domains induced by nanoscratch under 100 mN load. (**E**) Antiparallel nanoscratches before annealing. The red arrows indicate the directions of nanoscratches. (**F**) Optical image displaying the high-density stripe domains induced by antiparallel nanoscratches after annealing and chemical etching. (**G**) AFM scanning of the red-boxed region. (**H**) Detailed AFM scanning in the black-boxed region. (**I**) Vortex cores gathering near the nanoscratch. (**J**) Fast Fourier transform of (H).

fig. S10. A mono-chiral topological stripe domain is formed (*38*, *41*), due to elongated vortex-antivortex pairs as revealed in fig. S12. The range of high-density mono-chiral stripe domains can reach up to 50 μm in width (spacing between antiparallel nanoscratches) and extend across the entire crystal surface in length. Unlike antiparallel nanoscratches, parallel nanoscratches induce a herringbone domain distribution (fig. S13). The vortex cores are pushed into the middle region of the herringbone domain pattern, which also can be predicted via the strategy. In addition, the spacing of the parallel nanoscratches also affects the herringbone domain distribution (fig. S14).

DISCUSSION

To reveal the details of the strain generated by nanoscratch, we perform Raman spectroscopy measurement, which offers a unique possibility to detect strain at the micrometer scales by analyzing the offset of the characteristic peak position of deformed or strained material. After the nanoscratch, we select a set of points (1 to 11) with identical spacing and two more points (12 and 13) at a relatively large distance from the nanoscratch to perform Raman measurements, as marked in the inset of Fig. 4A. The strain distribution at different points can be quantitatively compared through the shift of the strongest scattering peaks (A_1 mode) in Fig. 4 (B and C), which reflect the stretching vibration mode of the apical oxygens of the MnO_5 polyhedron (*42*–*45*). The Raman shift of the A_1 mode and the corresponding positions are drawn in Fig. 4A. As we expected, the A_1 mode Raman shift is lower at the position closer to the nanoscratch, indicating that the tensile strain is larger. Compared with the A_1 mode Raman shift in the strain-free state, the A_1 mode Raman shift at sites 12 and 13, which are away from the nanoscratch, is stable at around 689 cm^{-1}, indicating that there is a small tensile strain independent of the nanoscratch existing in as-grown crystal.

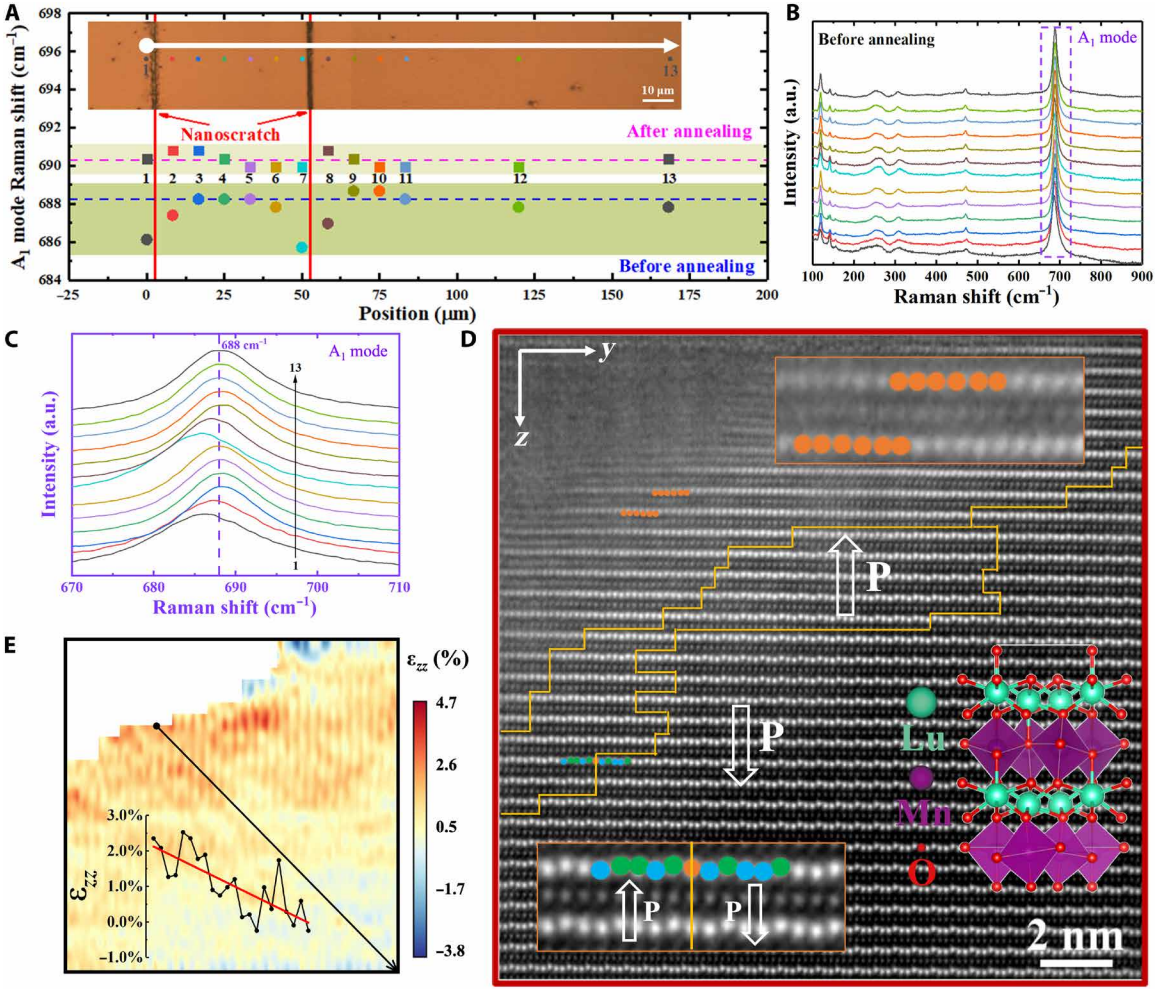

Fig. 4. Strain induced by nanoscratch. (**A**) Variation of A_1 mode near nanoscratch before and after annealing. The inset shows the position relationship between Raman test points and the double nanoscratches. (**B**) Raman spectra of 13 different positions near the nanoscratch on *ab* plane. (**C**) Enlarged view of the A_1 mode in the Raman spectra (B). (**D**) Atomically resolved HAADF image acquired near the nanoscratch on the *ac* plane. The brighter atom columns correspond to Lu columns. (Among them, Lu atoms offset in the +*z* direction, not offset, and offset in the −*z* direction are marked with green, orange, and blue circles, respectively.) The other atom type is Mn, while the O columns are invisible due to the *z*-contrast sensitivity of HAADF imaging. The yellow lines represent domain walls. The white arrows indicate the direction of polarization (P). The inset shows the $P6_3cm$ crystal structure of $LuMnO_3$. (**E**) Strain ε_{zz} map calculated by Lu atomic position. Inset: The ε_{zz} is plotted as a function of position along the black arrow.

Note that the tensile strain of all measured locations is relaxed after the annealing process, with the A_1 mode Raman shift returned to 691 cm^{-1}, as illustrated in fig. S15.

Next, we study the residual strain under the nanoscratch by STEM. Figure 4D shows a high-angle annular dark-field (HAADF) image viewed along the [010] zone axis (the location is at the yellow-boxed region in fig. S16A). It can be clearly seen that the lattice has distorted notably near the nanoscratch, and the positions of Lu atoms are visually flattened, as indicated by the upper orange-boxed region in Fig. 4D. This phenomenon may be attributed to a sufficiently large strain that changes the structure into nonpolar phase near the edge. It is also possible that the atoms in the fresh surface produced by the scratches are restructured so that the shielding mechanism suppresses its ferroelectricity (*46*). Different from the surface, the inside shows a standard ferroelectric domain with "up-up-down" (upward polarization) and "down-down-up" (downward polarization) arrangements. The corresponding strain distribution according to the Lu positions can be obtained in fig. S16B and Fig. 4E. The details for strain calculation can be found in Materials and Methods. Atomic-resolved strain distribution confirms that the nanoscratch mainly has tensile strain. The strain gradually relaxes as it moved away from the nanoscratch. A similar tendency is also confirmed by Mn atom strain calculation in fig. S17. It is worth mentioning that a large strain at the edge of the nanoscratch causes sample damage, which is evident in fig. S16C. Compared with the range (~20 μm on *ab* plane) of strain obtained by Raman, the range of strain is about 20 nm along the *c* axis below the nanoscratch. Therefore, the strain decays slower on the *ab* plane than that along the *c* axis by about three orders of magnitude, mainly due to the layered structure of hexagonal manganites. Therefore, the strain on the *ab* plane plays a major role in regulating vortex domain distribution.

To sum up, we propose and demonstrate a mechanical designable strategy to manipulate the alignment of topological domain networks. Different from the change of ferroelectric domain configuration by nanoindentation in $BaTiO_3$, which is derived from stress-generated cracks and slip band–induced ferroelastic response (*47*), our experiments and simulations suggest that the hexagonal crystalline structure and the strain field around the indent dominate the domain evolution. Compared with the random crack–induced oriented domain pattern during the crystal quenching process, the artificial nanoindentation and nanoscratch demonstrate a deterministic method to induce the topological mono-chiral stripes (*48*). We also want to emphasize that the nanoindentation/nanoscratch strategy can be potentially extended to other structural distortions dominating improper ferroelectrics or structural-sensitive magnetic materials (*49*). Compared with the dislocation generation strategy (*50*, *51*), we have achieved a designable local precise regulation approach through nanoscratches. The successful achievement of high-density parallel stripe domains in hexagonal manganites with a width of 50 μm, periodicity of 400 nm, and an extendable length according to the nanoscratch length creates a playground for the fascinating half-wave rectification effect (*29*) and microwave conductivity (*52*) of high-frequency AC signal functionalities at domain wall. A macroscopic enhancement of domain wall functionalities is expected as well. Note that the formed topological protected high-density stripe domains may notably alter the anisotropic physical properties, such as thermal conductivity and electrical conductivity. In addition, the domain periodicity width (~400 nm), which is in the wavelength range of visible light, and periodically polarization, which is comparable to artificial superlattices, may be developed for applications in such periodically poled lithium niobate (PPLN)–based devices as optical gratings and optical modulators.

MATERIALS AND METHODS

$LuMnO_3$ single-crystal growth

Using Lu_2O_3 and MnO_2 as raw materials and Bi_2O_3 as the solvent, flake $LuMnO_3$ single crystals were grown by flux method. The raw materials were mixed and transferred to a platinum crucible, heated from room temperature to 1280°C holding for 3 hours. The single crystals were crystallized in the slow cooling process. The as-grown $LuMnO_3$ single crystal is centimeter-size and plate-like.

Nanoindentation and nanoscratch

Nanoindentation and nanoscratch were performed using a commercial In Situ Nanomechanical Test System (Keysight G200) with Berkovich and spherical indenters. The Berkovich diamond indenter has a tip radius of 20 nm with a hardness of 1140 GPa. The spherical diamond indenter has a diameter of 650 μm with a hardness of 1140 GPa.

Scanning probe microscopy

Scanning probe microscopy (SPM) measurements were performed using a commercial atomic force microscope (AFM; Asylum Research MFP-3D). AFM measurements were performed by AC air topography mode with Si AC160TS-R3 cantilever tips (no coating) with a radius of ~7 nm and spring constants of 26 N/m. Piezoelectric force microscope (PFM) measurements were performed by single-frequency PFM mode with Si ASYELEC-01-R2 cantilever tips (coating Ti/Ir) with a radius of ~25 nm and spring constants of 2.8 N/m.

Optical microscope

Ferroelectric domain images in bright field and dark field are obtained using a commercial microscope ZEISS Axio Imager 2.

Scanning transmission electron microscopy

STEM images were performed on the cross section of nanoscratch obtained by focusing ion beam (FIB) technology. HAADF images were recorded at 300 kV using an aberration-corrected FEI Titan Themis G2. The convergence semiangle for imaging was 30 mrad, and the collection semiangle snap range was 39 to 200 mrad for HAADF imaging. To obtain quantitative information on the strain distribution, the atomic positions were determined by simultaneous fitting with two-dimensional Gaussian peaks using a MATLAB code.

Raman measurement

Raman measurements were performed using a commercial imaging spectrometer (HORIBA Ltd., iHR550) with a 633-nm excitation laser. The laser beam power density was low enough to avoid laser heating. The propagation of the laser beam was along the *c* axis of $LuMnO_3$ samples.

Supplementary Materials

This PDF file includes:

Supplementary Text
Figs. S1 to S17
Table S1
References

REFERENCES AND NOTES

1. N. D. Mermin, The topological theory of defects in ordered media. *Rev. Mod. Phys.* **51**, 591–648 (1979).
2. S. Z. Lin, X. Y. Wang, Y. Kamiya, G. W. Chern, F. Fan, D. Fan, B. Casas, Y. Liu, V. Kiryukhin, W. H. Zurek, C. D. Batista, S. W. Cheong, Topological defects as relics of emergent continuous symmetry and Higgs condensation of disorder in ferroelectrics. *Nat. Phys.* **10**, 970–977 (2014).
3. Q. N. Meier, M. Lilienblum, S. M. Griffin, K. Conder, E. Pomjakushina, Z. Yan, E. Bourret, D. Meier, F. Lichtenberg, E. K. H. Salje, N. A. Spaldin, M. Fiebig, A. Cano, Global formation of topological defects in the multiferroic hexagonal manganites. *Phys. Rev. X* **7**, 041014 (2017).
4. G. F. Nataf, M. Guennou, J. M. Gregg, D. Meier, J. Hlinka, E. K. H. Salje, J. Kreisel, Domain-wall engineering and topological defects in ferroelectric and ferroelastic materials. *Nat. Rev. Phys.* **2**, 634–648 (2020).
5. Y. Dai, Z. Zhou, A. Ghosh, R. S. K. Mong, A. Kubo, C. B. Huang, H. Petek, Plasmonic topological quasiparticle on the nanometre and femtosecond scales. *Nature* **588**, 616–619 (2020).
6. I. Kolvin, G. Cohen, J. Fineberg, Topological defects govern crack front motion and facet formation on broken surfaces. *Nat. Mater.* **17**, 140–144 (2018).
7. T. B. Saw, A. Doostmohammadi, V. Nier, L. Kocgozlu, S. Thampi, Y. Toyama, P. Marcq, C. T. Lim, J. M. Yeomans, B. Ladoux, Topological defects in epithelia govern cell death and extrusion. *Nature* **544**, 212–216 (2017).
8. A. S. Meeussen, E. C. Oğuz, Y. Shokef, M.v. Hecke., Topological defects produce exotic mechanics in complex metamaterials. *Nat. Phys.* **16**, 307–311 (2020).
9. I. I. Naumov, L. Bellaiche, H. Fu, Unusual phase transitions in ferroelectric nanodisks and nanorods. *Nature* **432**, 737–740 (2004).
10. W. Yang, G. Tian, Y. Zhang, F. Xue, D. Zheng, L. Zhang, Y. Wang, C. Chen, Z. Fan, Z. Hou, D. Chen, J. Gao, M. Zeng, M. Qin, L. Q. Chen, X. Gao, J. M. Liu, Quasi-one-dimensional metallic conduction channels in exotic ferroelectric topological defects. *Nat. Commun.* **12**, 1306 (2021).
11. Z. Hou, Y. Wang, X. Lan, S. Li, X. Wan, F. Meng, Y. Hu, Z. Fan, C. Feng, M. Qin, M. Zeng, X. Zhang, X. Liu, X. Fu, G. Yu, G. Zhou, Y. Zhou, W. Zhao, X. Gao, J. M. Liu, Controlled switching of the number of skyrmions in a magnetic nanodot by electric fields. *Adv. Mater.* **34**, e2107908 (2022).
12. A. Mesaros, K. Fujita, H. Eisaki, S. Uchida, J. C. Davis, S. Sachdev, J. Zaanen, M. J. Lawler, E. A. Kim, Topological defects coupling smectic modulations to intra-unit-cell nematicity in cuprates. *Science* **333**, 426–430 (2011).
13. H. Yang, B. Shen, Z. Wang, L. Shan, C. Ren, H.-H. Wen, Vortex images on $Ba_{1-x}K_xFe_2As_2$ observed directly by magnetic force microscopy. *Phys. Rev. B* **85**, 014524 (2012).
14. P. Milde, D. Kohler, J. Seidel, L. M. Eng, A. Bauer, A. Chacon, J. Kindervater, S. Muhlbauer, C. Pfleiderer, S. Buhrandt, C. Schutte, A. Rosch, Unwinding of a skyrmion lattice by magnetic monopoles. *Science* **340**, 1076–1080 (2013).
15. C. Donnelly, K. L. Metlov, V. Scagnoli, M. Guizar-Sicairos, M. Holler, N. S. Bingham, J. Raabe, L. J. Heyderman, N. R. Cooper, S. Gliga, Experimental observation of vortex rings in a bulk magnet. *Nat. Phys.* **17**, 316–321 (2021).
16. E. D. Roede, K. Shapovalov, T. J. Moran, A. B. Mosberg, Z. Yan, E. Bourret, A. Cano, B. D. Huey, A. T. J. van Helvoort, D. Meier, The third dimension of ferroelectric domain walls. *Adv. Mater.* **34**, e2202614 (2022).
17. H. Simons, A. B. Haugen, A. C. Jakobsen, S. Schmidt, F. Stohr, M. Majkut, C. Detlefs, J. E. Daniels, D. Damjanovic, H. F. Poulsen, Long-range symmetry breaking in embedded ferroelectrics. *Nat. Mater.* **17**, 814–819 (2018).
18. D. Meier, J. Seidel, M. Gregg, R. Ramesh. *Domain Walls: From Fundamental Properties to Nanotechnology Concepts* (Oxford Univ. Press, 2020).
19. D. Meier, S. M. Selbach, Ferroelectric domain walls for nanotechnology. *Nat. Rev. Mater.* **7**, 157–173 (2022).
20. Z. Hong, S. Das, C. Nelson, A. Yadav, Y. Wu, J. Junquera, L. Q. Chen, L. W. Martin, R. Ramesh, Vortex domain walls in ferroelectrics. *Nano Lett.* **21**, 3533–3539 (2021).
21. J. Seidel. *Topological Structures in Ferroic Materials* (Springer, 2016).
22. S. Das, Y. L. Tang, Z. Hong, M. A. P. Goncalves, M. R. McCarter, C. Klewe, K. X. Nguyen, F. Gomez-Ortiz, P. Shafer, E. Arenholz, V. A. Stoica, S. L. Hsu, B. Wang, C. Ophus, J. F. Liu, C. T. Nelson, S. Saremi, B. Prasad, A. B. Mei, D. G. Schlom, J. Iniguez, P. Garcia-Fernandez, D. A. Muller, L. Q. Chen, J. Junquera, L. W. Martin, R. Ramesh, Observation of room-temperature polar skyrmions. *Nature* **568**, 368–372 (2019).
23. L. Zhou, Y. Huang, S. Das, Y. Tang, C. Li, H. Tian, L.-Q. Chen, Y. Wu, R. Ramesh, Z. Hong, Local manipulation and topological phase transitions of polar skyrmions. *Matter* **5**, 1031–1041 (2022).
24. C. Feng, F. Meng, Y. Wang, J. Jiang, N. Mehmood, Y. Cao, X. Lv, F. Yang, L. Wang, Y. Zhao, S. Xie, Z. Hou, W. Mi, Y. Peng, K. Wang, X. Gao, G. Yu, J. Liu, Field-free manipulation of skyrmion creation and annihilation by tunable strain engineering. *Adv. Funct. Mater.* **14**, 2008715 (2021).
25. Y. J. Wang, Y. P. Feng, Y. L. Zhu, Y. L. Tang, L. X. Yang, M. J. Zou, W. R. Geng, M. J. Han, X. W. Guo, B. Wu, X. L. Ma, Polar meron lattice in strained oxide ferroelectrics. *Nat. Mater.* **19**, 881–886 (2020).
26. F. Fan, Z. Gao, L. Ponet, J. Wang, H. Huang, S. Artyukhin, J. Hong, S.-W. Cheong, X. Wang, Visualization of large-scale charged domain walls in hexagonal manganites. *Appl. Phys. Lett.* **118**, 072901 (2021).
27. D. Meier, J. Seidel, A. Cano, K. Delaney, Y. Kumagai, M. Mostovoy, N. A. Spaldin, R. Ramesh, M. Fiebig, Anisotropic conductance at improper ferroelectric domain walls. *Nat. Mater.* **11**, 284–288 (2012).
28. W. Wu, Y. Horibe, N. Lee, S. W. Cheong, J. R. Guest, Conduction of topologically protected charged ferroelectric domain walls. *Phys. Rev. Lett.* **108**, 077203 (2012).
29. J. Schaab, S. H. Skjaervo, S. Krohns, X. Dai, M. E. Holtz, A. Cano, M. Lilienblum, Z. Yan, E. Bourret, D. A. Muller, M. Fiebig, S. M. Selbach, D. Meier, Electrical half-wave rectification at ferroelectric domain walls. *Nat. Nanotechnol.* **13**, 1028–1034 (2018).
30. X. Wu, U. Petralanda, L. Zheng, Y. Ren, R. Hu, S. W. Cheong, S. Artyukhin, K. Lai, Low-energy structural dynamics of ferroelectric domain walls in hexagonal rare-earth manganites. *Sci. Adv.* **3**, e1602371 (2017).
31. P. W. Turner, J. P. V. McConville, S. J. McCartan, M. H. Campbell, J. Schaab, R. G. P. McQuaid, A. Kumar, J. M. Gregg, Large carrier mobilities in $ErMnO_3$ conducting domain walls revealed by quantitative Hall-effect measurements. *Nano Lett.* **18**, 6381–6386 (2018).
32. M. P. Campbell, J. P. McConville, R. G. McQuaid, D. Prabhakaran, A. Kumar, J. M. Gregg, Hall effect in charged conducting ferroelectric domain walls. *Nat. Commun.* **7**, 13764 (2016).
33. X. Y. Wang, F. T. Huang, R. W. Hu, F. Fan, S. W. Cheong, Self-poling with oxygen off-stoichiometry in ferroelectric hexagonal manganites. *APL Mater.* **3**, 041505 (2015).
34. M. G. Han, Y. Zhu, L. Wu, T. Aoki, V. Volkov, X. Wang, S. C. Chae, Y. S. Oh, S. W. Cheong, Ferroelectric switching dynamics of topological vortex domains in a hexagonal manganite. *Adv. Mater.* **25**, 2415–2421 (2013).
35. S. Artyukhin, K. T. Delaney, N. A. Spaldin, M. Mostovoy, Landau theory of topological defects in multiferroic hexagonal manganites. *Nat. Mater.* **13**, 42–49 (2014).
36. S. C. Chae, Y. Horibe, D. Y. Jeong, S. Rodan, N. Lee, S. W. Cheong, Self-organization, condensation, and annihilation of topological vortices and antivortices in a multiferroic. *Proc. Natl. Acad. Sci. U.S.A.* **107**, 21366–21370 (2010).
37. Q. Zhang, G. Tan, L. Gu, Y. Yao, C. Jin, Y. Wang, X. Duan, R. Yu, Direct observation of multiferroic vortex domains in $YMnO_3$. *Sci. Rep.* **3**, 2741 (2013).
38. X. Wang, M. Mostovoy, M. G. Han, Y. Horibe, T. Aoki, Y. Zhu, S. W. Cheong, Unfolding of vortices into topological stripes in a multiferroic material. *Phys. Rev. Lett.* **112**, 247601 (2014).
39. O. W. Sandvik, A. M. Muller, H. W. Anes, M. Zahn, J. He, M. Fiebig, T. Lottermoser, T. Rojac, D. Meier, J. Schultheiss, Pressure control of nonferroelastic ferroelectric domains in $ErMnO_3$. *Nano Lett.* **23**, 6994–7000 (2023).
40. R. G. P. McQuaid, M. P. Campbell, R. W. Whatmore, A. Kumar, J. M. Gregg, Injection and controlled motion of conducting domain walls in improper ferroelectric Cu-Cl boracite. *Nat. Commun.* **8**, 15105 (2017).
41. M.-G. Han, J. Li, F. Xue, X. Wang, Q.-P. Meng, J. Tao, L.-Q. Chen, S.-W. Cheong, Y. Zhu, Linearly aligned single-chiral vortices in hexagonal manganites by in situ electric arc heating. *Phys. Rev. Mater.* **2**, 064004 (2018).
42. M. N. Iliev, H. G. Lee, V. N. Popov, M. V. Abrashev, A. Hamed, R. L. Meng, C. W. Chu, Raman- and infrared-active phonons in hexagonal YMnO 3: Experiment and lattice-dynamical calculations. *Phys. Rev. B* **56**, 2488–2494 (1997).
43. H. Fukumura, S. Matsui, H. Harima, K. Kisoda, T. Takahashi, T. Yoshimura, N. Fujimura, Raman scattering studies on multiferroic $YMnO_3$. *J. Phys. Condens. Matter* **19**, 365239 (2007).
44. J. Vermette, S. Jandl, A. A. Mukhin, V. Y. Ivanov, A. Balbashov, M. M. Gospodinov, L. Pinsard-Gaudart, Raman study of the antiferromagnetic phase transitions in hexagonal $YMnO_3$ and $LuMnO_3$. *J. Phys. Condens. Matter* **22**, 356002 (2010).
45. S. Cheng, M. Li, S. Deng, S. Bao, P. Tang, W. Duan, J. Ma, C. Nan, J. Zhu, Manipulation of magnetic properties by oxygen vacancies in multiferroic $YMnO_3$. *Adv. Funct. Mater.* **26**, 3589–3598 (2016).
46. S. Deng, S. Cheng, C. Xu, B. Ge, X. Sun, R. Yu, W. Duan, J. Zhu, Atomic mechanism of hybridization-dependent surface reconstruction with tailored functionality in hexagonal multiferroics. *ACS Appl. Mater. Interfaces* **9**, 27322–27331 (2017).
47. G. A. Schneider, T. Scholz, J. Muñoz-Saldaña, M. V. Swain, Domain rearrangement during nanoindentation in single-crystalline barium titanate measured by atomic force microscopy and piezoresponse force microscopy. *Appl. Phys. Lett.* **86**, 192903 (2005).
48. M. Lilienblum. "Ferroelectric order in multiferroic hexagonal mangnites". thesis, Eidgenössische Technische Hochschule Zürich, (2016).
49. J. Zhang, W. K. Lee, R. Tu, D. Rhee, R. Zhao, X. Wang, X. Liu, X. Hu, X. Zhang, T. W. Odom, M. Yan, Spontaneous formation of ordered magnetic domains by patterning stress. *Nano Lett.* **21**, 5430–5437 (2021).
50. M. Hofling, X. Zhou, L. M. Riemer, E. Bruder, B. Liu, L. Zhou, P. B. Groszewicz, F. Zhuo, B. X. Xu, K. Durst, X. Tan, D. Damjanovic, J. Koruza, J. Rodel, Control of polarization in bulk ferroelectrics by mechanical dislocation imprint. *Science* **372**, 961–964 (2021).

51. M. Höfling, M. Trapp, L. Porz, H. Uršič, E. Bruder, H.-J. Kleebe, J. Rödel, J. Koruza, Large plastic deformability of bulk ferroelectric $KNbO_3$ single crystals. *J. Eur. Ceram. Soc.* **41**, 4098–4107 (2021).
52. X. Wu, K. Du, L. Zheng, D. Wu, S.-W. Cheong, K. Lai, Microwave conductivity of ferroelectric domains and domain walls in a hexagonal rare-earth ferrite. *Phys. Rev. B* **98**, 081409 (R) (2018).
53. A.C. Fischer-Cripps. *Introduction to Contact Mechanics* (Mechanical Engineering Series, Springer, 2007).
54. X. D. Han, K. Zheng, Y. F. Zhang, X. N. Zhang, Z. Zhang, Z. L. Wang, Low-temperature in situ large-strain plasticity of silicon nanowires. *Adv. Mater.* **19**, 2112–2118 (2007).
55. Y. Yue, P. Liu, Z. Zhang, X. Han, E. Ma, Approaching the theoretical elastic strain limit in copper nanowires. *Nano Lett.* **11**, 3151–3155 (2011).
56. M. Wu, X. Zhang, X. Li, K. Qu, Y. Sun, B. Han, R. Zhu, X. Gao, J. Zhang, K. Liu, X. Bai, X. Z. Li, P. Gao, Engineering of atomic-scale flexoelectricity at grain boundaries. *Nat. Commun.* **13**, 216 (2022).
57. J. Nordlander, M. Campanini, M. D. Rossell, R. Erni, Q. N. Meier, A. Cano, N. A. Spaldin, M. Fiebig, M. Trassin, The ultrathin limit of improper ferroelectricity. *Nat. Commun.* **10**, 5591 (2019).
58. F. T. Huang, X. Wang, S. M. Griffin, Y. Kumagai, O. Gindele, M. W. Chu, Y. Horibe, N. A. Spaldin, S. W. Cheong, Duality of topological defects in hexagonal manganites. *Phys. Rev. Lett.* **113**, 267602 (2014).
59. J. A. Mundy, J. Schaab, Y. Kumagai, A. Cano, M. Stengel, I. P. Krug, D. M. Gottlob, H. Dog Anay, M. E. Holtz, R. Held, Z. Yan, E. Bourret, C. M. Schneider, D. G. Schlom, D. A. Muller, R. Ramesh, N. A. Spaldin, D. Meier, Functional electronic inversion layers at ferroelectric domain walls. *Nat. Mater.* **16**, 622–627 (2017).
60. S. B. Cheng, Q. P. Meng, M. G. Han, S. Q. Deng, X. Li, Q. H. Zhang, G. T. Tan, G. A. Botton, Y. M. Zhu, Revealing the effects of trace oxygen vacancies on improper ferroelectric manganite with in situ biasing. *Adv. Electron. Mater.* **5**, 1800827 (2019).
61. T. Wermelinger, C. Borgia, C. Solenthaler, R. Spolenak, 3-D Raman spectroscopy measurements of the symmetry of residual stress fields in plastically deformed sapphire crystals. *Acta Mater.* **55**, 4657–4665 (2007).
62. T. Wermelinger, R. Spolenak. *Confocal Raman Microscopy*, (Springer International Publishing, 2018), pp. 509–529.
63. L.D. Landau, E.M. Lifshitz. *Theory of Elasticity (Third Edition)* (Butterworth-Heinemann, 1986).

Acknowledgments

Funding: We acknowledge the support of the National Natural Science Foundation of China (92163101 and 12172047), the National Key Research and Development Program of China (2019YFA0307900 and 2021YFA1400300), and the Beijing Natural Science Foundation (Z190011). S.-W.C. was supported by the W. M. Keck Foundation grant to the Keck Center for Quantum Magnetism at Rutgers University. **Author contributions:** Xu.W., J.H., and S.-W.C. designed and supervised the experiments. Z.G. grew single crystals, prepared samples, and carried out SPM and OM experimental characterization. F.H., K.J., and Z.Q. carried out nanoindentation experiment. Y. Zhang and H.H. provided the phase-field simulation. X.Z., Y.L., Yao Zhao, and Z.L. performed strain calculation. B.G. and Yi. Zhao performed finite element simulation. X.L. and P.G. performed STEM experimental characterization. Xi. Wang and X.C. prepared FIB samples. G.D. and Y.C. performed Raman experimental characterization. M.M. developed the mechanism analysis. All authors discussed the results and commented on the manuscript. **Competing interests:** The authors declare that they have no competing interests. **Data and materials availability:** All data needed to evaluate the conclusions in the paper are present in the paper and/or the Supplementary Materials.

Submitted 5 May 2023
Accepted 1 December 2023
Published 3 January 2024
10.1126/sciadv.adi5894